Gabor nonstationary deconvolution for attenuation compensation in highly lossy dispersive media

Kay Y. Liu, Elise C. Fear, and Mike E. Potter

ABSTRACT

Gabor nonstationary deconvolution was developed in the field of Seismology to compensate for attenuation loss, correct phase dispersion, and produce images with high resolution. Compared to seismic waves, a stronger attenuation and dispersion effect is observed in microwave frequency electromagnetic (EM) waves, especially with the propagating medium that has high loss and high dispersion, such as human body tissues. In the microwave image, it is displayed as a characteristic blurriness or lack of resolution that increases with time/distance. To produce microwave images with high resolution, there is a strong need for a technique that is able to compensate for the energy loss and correct for the wavelet distortion. Therefore, the Gabor algorithm is proposed to deal with the nonstationarity in EM wave propagation and attenuation. Gabor deconvolution is essentially based on the assumption that the anelastic attenuation of seismic waves can be described by a constant Q theory. Our study reveals that the same definition of Q as in seismic can also be used to characterize EM wave propagation and attenuation. Even though the Q for EM waves is not constant over the microwave frequency of interest; however, a parameter Q*, which is closely related to Q, can be approximated as constant for highly lossy dispersive human body tissues. Q and Q* might be different in the order of magnitude; however, these quantities describe the attenuation and dispersion in the same manner. Our test results indicate that Gabor nonstationary deconvolution is able to sufficiently compensate for attenuation loss and correct phase dispersion for EM waves that propagate through high lossy dispersive media. It can work effectively where a constant Q* approximation is achieved.

INTRODUCTION

Various inverse Q filtering techniques have been developed in the field of Seismology to compensate for energy loss, to correct for wavelet distortion in terms of shape and timing, and to produce an image with high resolution. Among these, the Gabor deconvolution method developed by (Margrave et al., 2011) has been successfully tested with industrial seismic data (Margrave et al., 2003, and Perz et al., 2005). The results indicate that, compared to the industry standard approach, Gabor deconvolution provides improved amplitude and phase content of certain seismic events. It is the purpose of this study to extend these findings to radar data, which necessitates a good understanding of the differences in the application conditions between the seismic waves and the EM waves, as well as the media being studied.

In particular, our study focuses on the tissue sensing adaptive radar (TSAR) system developed by (Fear et al., 2013) at the University of Calgary. The TSAR system uses low power microwave frequency electromagnetic (EM) waves to image the breast interior for tumor detection. Encouraging results have been obtained with simulation and phantom data, as well as some preliminary clinical exams. Those results indicate that TSAR images are able to detect the dielectric property changes in breast tissues. However, limited success

has been reported in imaging complicated model structures, i.e., targets within attenuating and dispersive heterogeneous media. The attenuation of EM waves in many biological materials is strongly dependent upon frequency in the microwave frequency range; higher frequencies are attenuated much more quickly than lower ones during propagation. As a result, the microwave wavelet often undergoes a significant change in shape as it travels through the media, and reflections received at later times are noticeably broader than those received at earlier times. In the microwave image, it is displayed as a characteristic blurriness or lack of resolution that increases with time/distance. There is a need for higher resolution and more sensitive microwave images in clinical applications. This triggered our interest in adapting Gabor nonstationary deconvolution to handle the nonstationarity in EM wave propagation and attenuation.

In essence, Gabor deconvolution is a natural extension of the standard Wiener deconvolution algorithm. It is based on the key assumption that, over the seismic frequencies of interest, the anelastic attenuation of seismic waves can be described by a constant Q theory (Kjartansson, 1979). Issues with this technique arise in light of the fact that, in our study, EM waves operate at the Gigahertz frequencies that are much higher than the frequencies of seismic waves. Secondly, human body tissues contain higher water content than geological materials. Thus, the wavelet attenuation and dispersion in EM wave propagation through the human body is more severe than that in seismic wave propagation through the earth subsurface. Moreover, extensive theoretical studies and experimental observations have provided evidence that constant Q is a reasonable approximation for seismic waves. A few researches have also been done on Q and Q* characterization of attenuation in ground penetrating radar (GPR) pulse for geophysical applications (Turner and Siggins, 1994, Bano, 1996, Irving and Knight, 2003, and Bradford, 2007). However, our literature studies reveal that no such work has been published for EM wave attenuation in highly lossy and dispersive biological tissues. The aim of this study is to investigate the Q characterization of EM wave propagation and attenuation in tissues, understand the frequency characteristics of Q in this context, and assess the ability of Gabor nonstationary deconvolution to deal with the attenuation and wavelet dispersion that are much more severe than those observed in seismic waves. Our theoretical derivations and experimental results demonstrate that (1) the same definition of Q can be found for seismic waves and EM waves; (2) the Q for EM waves varies with frequency; however, a parameter Q* can be found by taking the first order derivative of Q over frequency, which can be approximated as a constant over the microwave frequencies of interest; and (3) Gabor nonstationary deconvolution is able to remove the wavelet dispersion in the presence of high attenuation and dispersion.

The rest of this report is organized as follows. We start with a brief review of the concepts associated with EM wave propagation; then, explain the nonstationarity in the propagating wavelet due to the frequency-dependent attenuation. In Q Attenuation of EM Wave Propagation, the Q for EM waves is introduced and compared with the Q for seismic waves. We next apply Gabor nonstationary deconvolution to radar data that contains large attenuation and distortion. Selected results obtained with analytic, simulated, and measured data are demonstrated and discussed. At the end, conclusions are drawn based on those results and discussions.

ELECTROMAGNETIC WAVE PROPAGATION

Propagation Constants

We consider the simple case of uniform plane wave propagation in lossy and dispersive dielectric materials. The uniform plane wave solution for an electric field at a single frequency ω in one-dimension can be written in phasor form (Taflove and Hagness, 2000, and Pozar, 2005) as

$$E(t,x) = E_0 e^{i(\omega t - kx)}, \tag{1}$$

where t is the travel time, x is the travel distance, ω is the angular frequency, k is the complex wavenumber, and E_0 is the amplitude of the electric field at $x = 0$ an d $t = 0$. The complex wavenumber k is given by

$$k = \beta - i\alpha. \tag{2}$$

Parameters α and β are the attenuation and the phase terms, respectively, which are given by

$$\alpha(\omega) = \omega \sqrt{\frac{\mu_0 \varepsilon_{eff}(\omega)}{2}\left(\sqrt{1+\left(\frac{\sigma_{eff}(\omega)}{\omega \varepsilon_{eff}(\omega)}\right)^2} - 1\right)} \tag{3}$$

$$\beta(\omega) = \omega \sqrt{\frac{\mu_0 \varepsilon_{eff}(\omega)}{2}\left(\sqrt{1+\left(\frac{\sigma_{eff}(\omega)}{\omega \varepsilon_{eff}(\omega)}\right)^2} + 1\right)}. \tag{4}$$

The phase constant $\beta(\omega)$ is related to the phase velocity $v(\omega)$ by

$$v(\omega) = \frac{\omega}{\beta(\omega)}. \tag{5}$$

In (3) and (4), the constitutive parameter μ_0 is equal to the permeability of free space for most of the biological tissues. The frequency dependency of α and β is further complicated by the frequency dependency of the constitutive parameters ε_{eff} (effective permittivity) and σ_{eff} (effective conductivity).

Dielectric properties

The EM wave propagation in biological tissues is governed by the complex relative dielectric permittivity, ε^*, given by

$$\varepsilon^*(\omega) = \varepsilon'(\omega) - i\varepsilon''(\omega), \tag{6}$$

where ε' is the frequency-dependent dielectric constant which can be converted into the effective permittivity $\varepsilon_{eff}(\omega) = \varepsilon_0 \varepsilon'(\omega)$, and ε'' is the frequency-dependent dielectric loss which can be converted into the effective conductivity $\sigma_{eff}(\omega) = \omega \varepsilon_0 \varepsilon''(\omega)$. The

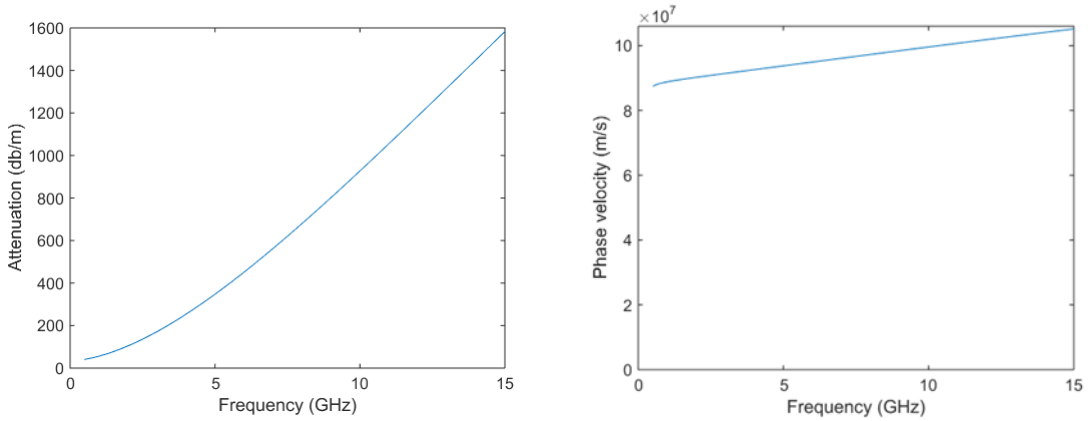

Fig. 1. Attenuation coefficient and phase velocity calculated for a selected human body tissue

constitutive parameter ε_0 is equal to the permittivity of free space.

The complex relative dielectric permittivity of tissues is often represented by the Cole-Cole model (Gabriel et al., 1996, and Lazebnik et al., 2007):

$$\varepsilon^*(\omega) = \varepsilon_\infty + \sum_{j=1}^{n} \frac{\varepsilon_{S,j} - \varepsilon_\infty}{1 + (i\omega\tau_j)^{1-\alpha_j}} + \frac{\sigma_S}{i\omega\varepsilon_0} \qquad (7)$$

in which n is the number of poles, τ_j, ε_∞, $\varepsilon_{S,j}$, α_j, and σ_S are the Cole-Cole model parameters that are estimated from the experimental data. τ_j is a generalized relaxation time to characterize the polarization mechanism in each of the relaxation regions. ε_∞ is the permittivity at the field frequencies where $\omega\tau_j \gg 1$, and $\varepsilon_{S,j}$ is the permittivity at $\omega\tau_j \ll 1$. σ_S is the static ionic conductivity. The distribution parameter α_j is a measure of the broadening of the dispersion and can assume values between 0 and 1. These parameters are estimated by fitting models to measurements of frequency dependent behavior obtained in laboratory tests and are used to determine attenuation rate and phase velocity.

Nonstationarity in EM wave propagation

Equations (3) and (5) indicate that, due to the frequency dependency of effective permittivity and conductivity, the attenuation constant and the phase velocity are also frequency-dependent. In Figure 1, using a human body tissue selected from (Gabriel et al., 1996) as an example, we plot the attenuation coefficient and the phase velocity as a function of frequency. In this example, the number of poles for the Cole-Cole formula in (7) is defined as n=4. It can be seen that the attenuation displays a high level of frequency dependency over the frequency range of interest. The plot shows an almost linear relationship between attenuation and frequency. On the other hand, the slow increase in velocity indicates that the change in shape of an EM pulse due to velocity dispersion alone will be minimal in this substance. These observations are consistent with those made from the propagation of subsurface radar pulse in geological materials (Irving and Knight, 2003).

From Fig. 1, the high-frequency components of the spectra travel with a higher velocity and are more quickly attenuated than the low frequency ones. The dissipative and dispersive effects caused by this frequency dependency introduce continuous changes in

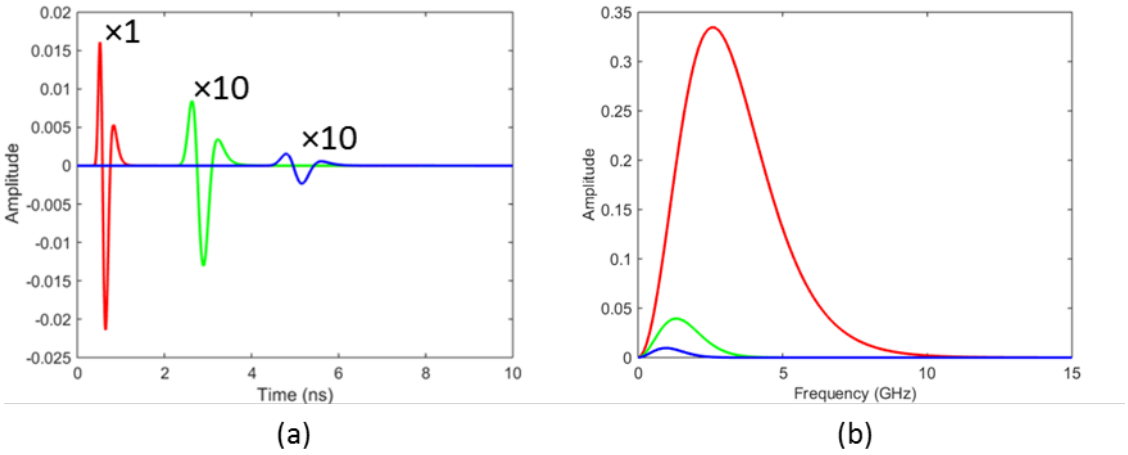

Fig. 2. A minimum phase wavelet traveling through the human body tissue shown in Figure 1. (a) Time domain signals. (b) Amplitude spectra. The color indicates the wavelet travel time: red is 0.5 ns, green is 2.5 ns, and blue is 4.5 ns.

both amplitude and phase spectra of the EM wavelet. As a result, the EM wavelet often undergoes a significant distortion in shape as it travels through the media, and the received signals at later times are noticeably broader than those received at earlier times. This phenomenon is illustrated by an analytical example shown in Figure 2, in which a minimum phase wavelet travels through the body tissue shown in Figure 1. For the time domain signals, the amplitude of the propagating wavelet at the two later travel locations has been amplified by 10 in order to make the waveform distortion more visible. It can be seen that, as the time delay increases, the wavelet broadens and its amplitude decreases; as well, there is a downshift in the peak frequency of the amplitude spectra.

The changes in the shape and bandwidth of the source wavelet due to the time-dependent frequency response is so called nonstationarity (Margrave et al., 2011). Therefore, of importance in this study are accounting for those significant distortions in the waveform, compensating for the energy attenuation to strengthen the response from the object of interest, deconvolving the propagating wavelet to improve the signal resolution, and achieving a high-resolution well-focused radar image for interpretation (i.e., diagnostic) purposes.

Q ATTENUATION OF EM WAVE PROPAGATION

Seismic attenuation is commonly characterized by the quality parameter Q. A variety of methods have been developed to estimate the earth Q function and reverse the earth Q effect on seismic waves. A good summary in this regard can be found in (Wang, 2008). Gabor nonstationary deconvolution (Margrave et al., 2011) is essentially based on the assumption that the effect of anelasticity on the wave propagation can be described by a constant Q theory (Kjartansson, 1979). To our knowledge, the Q characterization of EM wave attenuation in dielectric media has not yet been extensively studied and commonly applied. Therefore, in this section, we start with a brief review on Gabor nonstationary deconvolution; then, demonstrate that a similar parameter to the seismic Q does exist to describe the EM wave attenuation in the dielectric. Next, the mathematical definition of Q

for EM waves is derived. At the end, we compare the Q between the seismic wave and the EM wave in terms of the dissipation and dispersion scale and frequency-dependency. This comparison leads to a discussion on the potential challenges of applying Gabor nonstationary deconvolution to the media that are highly lossy and dispersive.

Gabor nonstationary deconvolution

Stationary deconvolution is fundamentally based on a stationary convolutional model. In its simplest form, this model is often stated as

$$s(t) = w(t) * r(t), \tag{8}$$

where $s(t)$ is the reflection measurement, $w(t)$ is the source wavelet, and $r(t)$ is the time domain reflectivity of the object under test. The stationary convolutional model assumes that the source wavelet propagates through a time-invariant system that has no distinction between the source wavelet and the propagating wavelet. Therefore, it is not able to account for nonstationarity in wave propagation.

In order to address this shortcoming in the stationary convolutional model, Gabor deconvolution is based on a nonstationary convolutional model, given by

$$s(t) = w(t) * b(t,\tau) * r(t), \tag{9}$$

in which τ is the travel time and $b(t,\tau)$ is the attenuation function describing the impulse response of the attenuation process for any travel time τ. The nonstationary convolutional model treats the source wavelet and the attenuation as separate effects. By estimating the attenuation function, we can remove it from the recorded signal; thus, the rest can be treated effectively by the stationary convolutional model. Therefore, nonstationary convolution is essentially a generalization of stationary convolution.

In Gabor deconvolution, the attenuation function is estimated in the Gabor domain based on the time-frequency decomposition of the recorded signal. For the nonstationary convolutional model defined in (9), the Gabor transform is given as

$$\hat{S}(f,\tau) \approx W(f)B(f,\tau)R(f,\tau), \tag{10}$$

where $\hat{S}(f,\tau)$ is the Gabor transform of recorded signal, $W(f)$ is the Fourier transform of source wavelet, $B(f,\tau)$ is the Fourier transform of attenuation function, and $R(f,\tau)$ is the Gabor transform of reflectivity. There are various ways to estimate the attenuation function in the Gabor domain. In particular, Margrave et al. (2002 and 2011) reported that the hyperbolic smoothing approach is robust and able to yield a more consistent estimate of the Gabor magnitude spectrum of the propagating wavelet. Hyperbolic smoothing is essentially based on the assumption that the nonstationary effects of attenuation are minimum phase and their Gabor magnitude spectra can be described by a constant Q as

$$|B(f,\tau)| = e^{\left(-\frac{\pi|f|\tau}{Q}\right)}. \tag{11}$$

For seismic waves, Q has been found to be largely frequency independent over a wide frequency range (Stacey et al., 1975, and Kjartansson, 1979). In the following sections, we will discuss Q in the context of EM wave propagation.

Q characterization of EM wave propagation

In EM applications, an important parameter to quantify the energy loss is the loss tangent, $tan\delta$. In particular, the loss tangent of the dielectric medium is defined as

$$tan\delta = \frac{\varepsilon^{"}}{\varepsilon'}, \tag{12}$$

where ε' and $\varepsilon^{"}$ correspond to the real and the imaginary parts of the complex relative permittivity defined in (6), respectively. As early as 1954, Von Hippel (1954) has associated the quality factor Q with the loss tangent to quantify the energy loss as EM waves propagate in the dielectric. He defined the Q as the inverse of the loss tangent, given by

$$Q = \frac{1}{tan\delta}. \tag{13}$$

Substituting (12) to (13), we get

$$Q = \frac{\varepsilon'}{\varepsilon^{"}}. \tag{14}$$

For an electric field of amplitude E_0, (14) can be rewritten as

$$Q = \frac{\frac{1}{2}\omega\varepsilon_0\varepsilon' E_0^2}{\frac{1}{2}\omega\varepsilon_0\varepsilon^{"} E_0^2}. \tag{15}$$

Given $\omega = 2\pi f$, $\varepsilon_{eff} = \varepsilon_0\varepsilon'$, and $\sigma_{eff} = \omega\varepsilon_0\varepsilon^{"}$, (15) can be rewritten as

$$Q = 2\pi f \frac{\frac{1}{2}\varepsilon_{eff} E_0^2}{\frac{1}{2}\omega\sigma_{eff} E_0^2}. \tag{16}$$

Define T as the duration of one wave cycle; thus, using T to replace the frequency, f, we have

$$Q = 2\pi \frac{\frac{1}{2}\varepsilon_{eff} E_0^2/T}{\frac{1}{2}\omega\sigma_{eff} E_0^2}, \tag{17}$$

which is equivalent to

$$Q = 2\pi \frac{Average\ energy\ stored\ per\ half\ cycle}{Energy\ dissipated\ per\ half\ cycle}. \tag{18}$$

This definition of Q is consistent with the one in (Kjartansson, 1979, Sheriff, 1984, and Aki and Richards, 2002) for characterizing the seismic attenuation, given as

$$Q = 2\pi \frac{Peak\ strain\ energy\ stored\ in\ volume}{Energy\ lost\ in\ each\ cycle}. \tag{19}$$

Mathematical definition of Q

Denote W as energy stored per cycle or per half cycle, and $-\Delta W$ as energy lost per cycle or per half cycle; thus, (18) and (19) can be simplified as

$$Q = -2\pi \frac{W}{\Delta W}. \tag{20}$$

Reorganizing (20), we get

$$\frac{2\pi}{Q} = -\frac{\Delta W}{W}. \tag{21}$$

The above definitions indicate that Q is inversely proportional to the attenuation. The smaller the value of Q, the greater the attenuation. However, these definitions are rarely of direct use since only in special experiments is it possible to measure the stored energy and the dissipated energy in each wave cycle or half wave cycle (Aki and Richards, 2002). Moreover, Stacey et al. (1975) pointed out that equation (21) refers to the situation in which the dissipated energy ΔW is much smaller than the stored energy W, i.e., $\Delta W/W \ll 1$. However, as EM waves propagate in body tissues, the condition of $\Delta W/W \ll 1$ is not always achieved. In order to deal with small Q values, we follow the same approach as in (Stacey et al., 1975) and convert (21) to the following differential form as

$$-\frac{2\pi}{Q} = \left(\frac{dW}{W}\right)\left(\frac{T}{dt}\right) = \left(\frac{T}{W}\right)\left(\frac{dW}{dt}\right). \tag{22}$$

Equation (22) implies that, for a propagating wave, we can follow the wave along and watch the energy diminish at a particular wave crest. In practice, this should also account for geometric spreading of wave on to a wider wave front. However, here we are dealing only with plane waves so that there is no diminution in amplitude or energy density due to geometrical spreading and the progressive decrease in energy density is due only to dielectric losses presented by (22).

For comparison with respect to observations, reference to wave amplitude 'E' rather than energy 'W' is generally preferred. It is widely accepted that

$$W \propto E^2, dW \propto 2EdE, \tag{23}$$

so that

$$\frac{dW}{W} = 2\frac{dE}{E}. \tag{24}$$

Substituting (24) to (22), we get

$$-\frac{\pi}{Q} = \left(\frac{T}{E}\right)\left(\frac{dE}{dt}\right). \tag{25}$$

Integration of equation (25) gives

$$E(t) = E_0 \exp\left(\frac{-\pi t}{QT}\right). \tag{26}$$

Alternatively, given λ as wavelength and v as wave velocity, we have $T = \lambda/v$ and $x = vt$. Thus, (26) can be written as

$$E(x) = E_0 \exp\left(\frac{-\pi}{Q\lambda}x\right) = E_0 \exp(-\alpha x), \tag{27}$$

where α is the attenuation coefficient. Therefore, Q and α can be associated by

$$Q = \frac{\omega}{2v\alpha}. \tag{28}$$

This relation is same as the one defined in (Aki and Richards, 2002) for seismic waves.

Comparison of Q for seismic waves and EM waves

Seismic imaging is based on the contrast in the viscoelastic properties of the earth subsurface materials. For most of the seismic applications, the frequency range of interest is between 5 Hz and 250 Hz. On the other hand, microwave imaging is based on the contrast in the dielectric properties of the materials, i.e., permittivity and conductivity. The associated EM wave propagates at a much higher frequency band than the seismic wave does. In particular, for the existing microwave breast imaging systems, the frequency of interest is normally between 500 MHz and 15 GHz. Because of these differences, the Q response to the propagating waves is also different. In particular, we are interested in: (1) the attenuation and dispersion of EM wave propagation in lossy dispersive body tissues relative to that of seismic wave propagation in geological materials; and (2) whether or not the constant Q model is an accurate description of EM wave attenuation over the microwave frequencies.

The definition of Q in (18) and (19) indicates that the value of Q is inversely proportional to the dissipated energy – the higher the attenuation, the smaller the value of Q. By (Sheriff, 1984), with geological materials, the values of Q are normally in the range of [50, 300] over the seismic frequencies. In order to quantify the range of Q for body tissues over microwave frequencies, we use the Cole-Cole formula defined in (7) to estimate the attenuation coefficient and phase velocity for a variety of human body tissues; then calculate the Q values based on (28). In the example shown in Figure 3, tissues (Gabriel et al., 1996) are selected based on their levels of water content. Higher water content indicates more attenuation. Among the demonstrated tissues, muscle has the highest water content, then followed by bone and fat. Our results reveal that, over the frequencies of microwave breast imaging, the Q lies somewhere between 1.5 and 8. This is more than an order of magnitude lower than the range of values typically given for seismic Q, which indicates that wavelet dissipation and dispersion is far more pronounced in radar data than in seismic data. Therefore, of importance in this study is the performance of Gabor nonstationary deconvolution in the presence of severe attenuation and dispersion.

On the other hand, the key to Gabor deconvolution is estimating the attenuation function, which is done via a hyperbolic smoothing approach. The fundamental assumption behind hyperbolic smoothing is that the nonstationary effects of attenuation can be depicted by the constant Q. For seismic waves, Q has been found to be largely frequency independent over a wide frequency range. For EM waves, the literature on GPR applications (Turner and Siggins, 1994, and Irving and Knight, 2003) has revealed that Q is not frequency independent over the bandwidth of a GPR wavelet. Consistent observations are also obtained from our calculations of Q for a variety of biological tissues and immersion media over the frequency range of existing microwave breast imaging systems. One of the examples is shown in Figure 3(c). In those conditions, even though Q is not constant over the examined frequency range, a useful observation is made that a region where Q is approximately linear with frequency can be found in a sub- band of frequency. This observation leads to the introduction of a new parameter Q* (Turner and

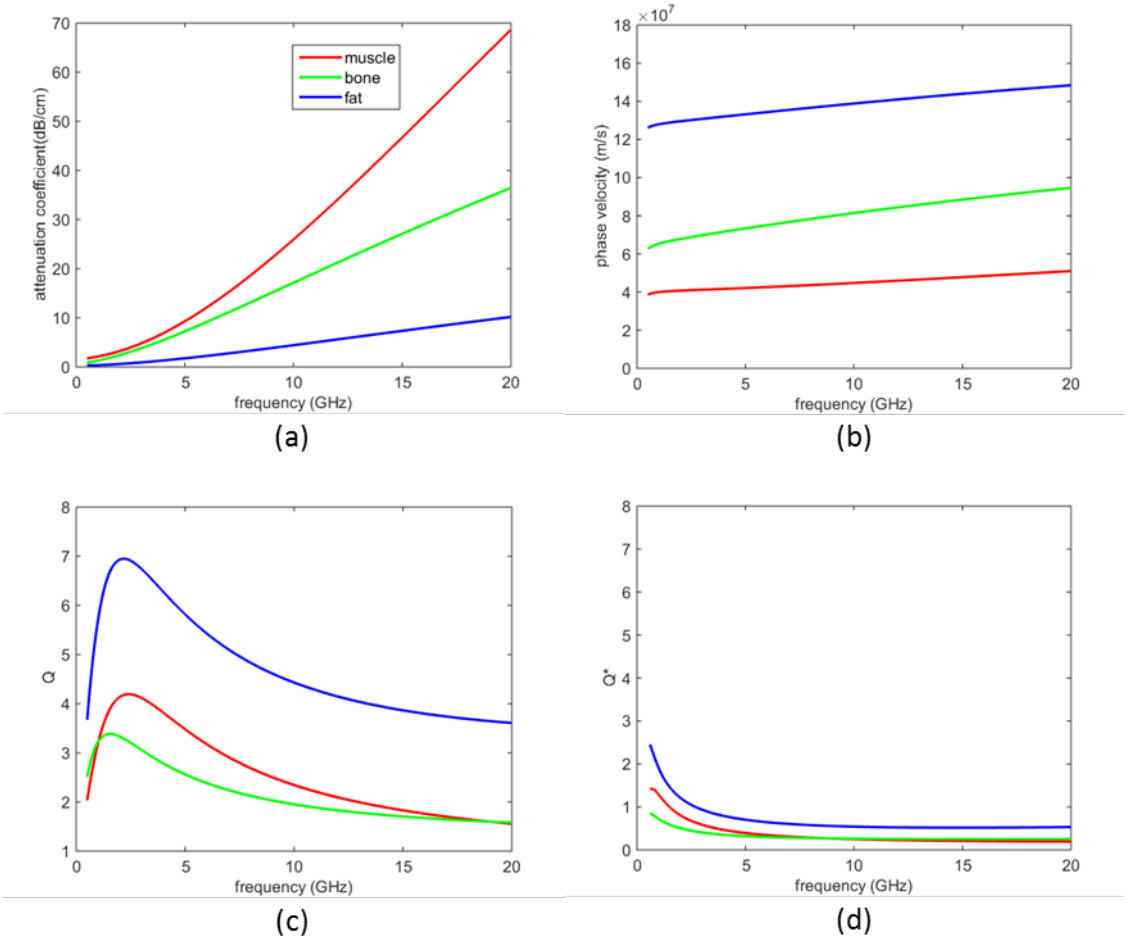

Fig. 3. Attenuation (a), velocity (b), Q (c), and Q* (d) calculated as a function of frequency for selected body tissues whose dielectric properties were fitted using the Cole-Cole formula: muscle is in red, bone is in green, and fat is in blue.

Siggins, 1994), defined as

$$Q^* = \frac{1}{2v}\left(\frac{d\alpha}{d\omega}\right)^{-1}, \tag{29}$$

in which the phase velocity v is approximated as a constant value over the frequency band of radar pulse, and $d\alpha/d\omega$ is the first order derivative of the attenuation coefficient with respect to the frequency. Equation (29) implies that, in the region where Q is approximately linear with frequency, a constant Q* can be approximated (shown in Figure 3(d)). Q and Q* might be different in the total amplitude; however, these quantities describe the same changes in wavelet shape that occur during propagation.

For hyperbolic smoothing, the importance of the frequency-dependency of Q is that it governs the shape of the hyperbolic contours for the attenuation function estimation. In Figure 4, using fatty tissue as an example, we compare the hyperbolas constructed with the constant Q and the frequency-dependent Q (i.e., the actual Q calculated using Cole-Cole model). The results indicate that the hyperbolic paths constructed with the constant Q model might result in under-compensation in certain areas on the time-frequency plane. In

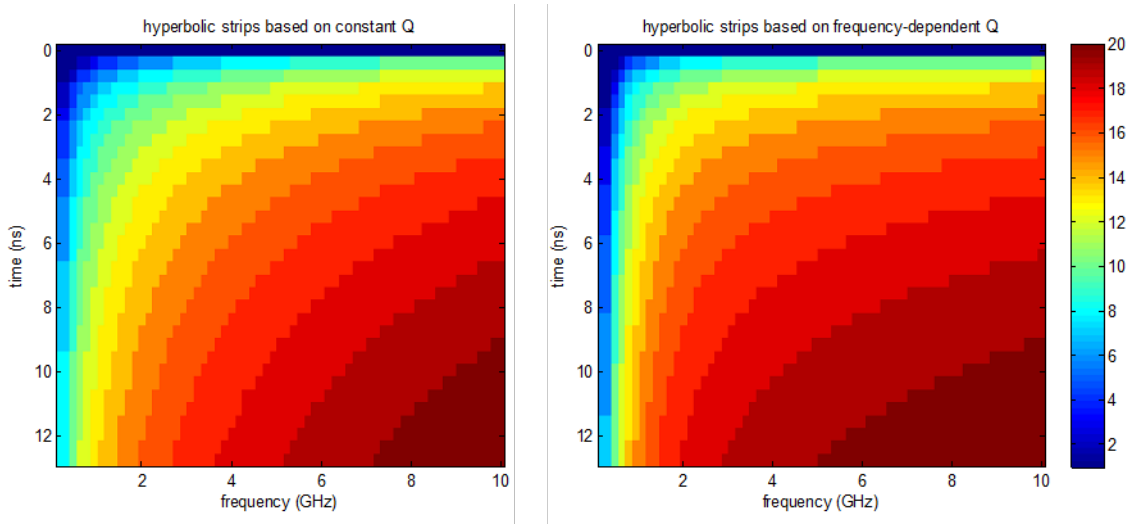

Fig. 4. Hyperbolic contours constructed in time-frequency domain with the constant Q model (left) and the frequency-dependent Q model (right).

this study, our interest is in the effect of this shape difference on the accuracy of the Gabor estimates. On the other hand, this study provides us with evidence in regard to the potential of applying Gabor deconvolution to the condition where a constant Q* is approximated.

DATA GENERATING AND PROCESSING

In this section, we describe the simulations and the experiments conducted to assess the performance of Gabor nonstationary deconvolution in the scenarios where EM waves propagate in highly lossy and dispersive dielectric materials.

Uniform plane wave propagation in lossy dispersive media

We first consider the simple case of uniform plane wave propagation in lossy and dispersive dielectric media. Our intention is to examine the ability of Gabor nonstationary deconvolution to compensate for attenuation loss and correct the phase dispersion. With uniform plane wave propagation, we can concentrate on the effects of attenuation and dispersion due to the dielectric properties, but eliminate the effects from other undesired factors (e.g., the attenuation due to geometric spreading in cylindrical or spherical wave propagation).

Given the uniform plane wave solution for an electric field in (1), we substitute the complex wave number in (2) to get

$$E(t,x) = E_0 e^{-\alpha x} e^{i(\omega t - \beta x)}. \tag{30}$$

Equation (30) indicates that, given a propagation location x, the wave attenuation at a single frequency ω can be written as

$$b(t,x) = e^{-\alpha x} e^{i(\omega t - \beta x)}. \tag{31}$$

Therefore, the impulse response of the attenuation process over a broad frequency range is given by

Table 1. Steps to generate synthetic signal

1) In frequency domain, use the Cole-Cole model to compute the attenuation coefficient and the phase velocity for the given medium at defined sampling frequencies.

2) Define a time sequence $t = \{t[i]\} = \{i\Delta t\}$, $i = 0, 1, .., N-1$, which includes N temporal sample points with a sample time interval of Δt.

3) Choose an arbitrary reference frequency ω_0. Use its phase velocity, v_0, to calculate the sequence of travel distance $x = \{x[i]\} = \{i\Delta t v_0\}$, $i = 0, 1, .., N-1$.

4) Starting with $x[0]$, calculate the spectrum of attenuation function based on (34).

5) Multiply the spectrum of the source wavelet with the attenuation function to get the propagating wavelet at $x[0]$.

6) Inverse Fourier transform the spectrum of the propagating wavelet to time domain.

7) Repeat the steps 4 to 6 for each element in x to construct a matrix. The column vector of the matrix describes the waveform of the propagating wavelet at individual locations.

8) Generate a pseudo reflectivity series by either a random data generator or arbitrarily choosing location and amplitude for reflectivity.

9) Multiply the matrix constructed in step 7 with the pseudo reflectivity series to get the synthesized attenuated signal.

$$\int b(t,x)d\omega = \int (e^{-\alpha x}e^{-i\beta x})e^{i\omega t}d\omega, \tag{32}$$

which gives the Fourier transform of the impulse response as

$$B(\omega, x) = e^{-\alpha x}e^{-i\beta x}. \tag{33}$$

This definition relates to the attenuation function described in (Margrave et al., 2011). Replacing β in (33) with the phase velocity, we have

$$B(\omega, x) = e^{-\alpha x}e^{-i\frac{\omega}{v}x}. \tag{34}$$

Given the above derivations, the steps to generate the synthetic signal are described in Table 1.

In particular, frequency domain modeling practice is followed in order to generate the propagating wavelet at each travel distance. Firstly, the propagating wavelet is calculated in the frequency domain by multiplying the attenuation function with the source wavelet; then, the time domain signal is obtained via inverse Fourier transform. This is noted because, given the high loss and dispersion of biological tissues in the Gigahertz frequency range, artifacts can be introduced to the time domain representation of the attenuation function due to insufficient coverage of the low frequency components in the inverse

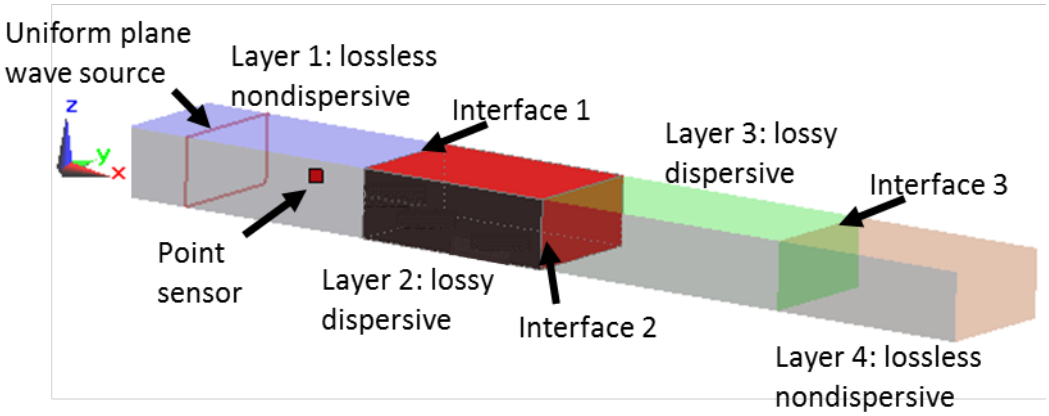

Fig. 5 Setup up of plane wave guide simulation. From left to right, the layers are numbered from 1 to 4. Interface 1 is between the layers 1 and 2, Interface 2 is between the layers 2 and 3, and Interface 3 is between the layers 3 and 4.

Fourier transform. By multiplying the spectra of the source wavelet and the attenuation function, the high magnitude at the low frequencies of attenuation function can be effectively filtered by the source wavelet, so that the artifacts existing in the inverse Fourier Transform of the attenuation function can be avoided.

Parallel plate waveguide simulations

A waveguide is a structure that confines and conveys EM waves or sounds waves. They enable a signal to propagate with minimal loss of energy. A variety of waveguide structures have been developed in microwave engineering. In particular, we use the parallel plane waveguide to simulate the plane wave propagation in the dielectrics. A series of simulations are conducted to explore the ability of Gabor nonstationary deconvolution to handle small valued and frequency-dependent Q. Unless specified, all the simulations in this paper are performed using SEMCAD X (SPEAG, Zürich, Switzerland), which utilizes the finite-difference-time-domain (FDTD) technique.

Figure 5 illustrates the setup of the parallel plate waveguide simulation. The object has a layered structure, including four homogeneous media. The plane wave source is placed in Layer 1 to generate wave propagation along the +x direction. In SEMCAD, the plane wave source has to be placed in a lossless and nondispersive medium in order to yield stabilized plane wave propagation. As well, a nondispersive medium is required on the boundary of the simulation space in order to achieve an absorption boundary condition. Therefore, in this paper, unless specified, layers 1 and 4 have dielectric properties of lossless nondispersive media with the effective permittivity equal to 2.5 and 1, respectively. The layers 2 and 3 are lossy and dispersive. Different dielectric properties are assigned to these layers in order to create different attenuation and dispersion effects. Figure 6 describes the dissipative and dispersive behavior of these layers in two different scenarios, one with mild loss and dispersion and the other with high loss and dispersion. As revealed by Figure 6(c), in either case, a low contrast is observed at the interface between these two layers. A point sensor is placed inside of Layer 1 between the plane wave source and the first interface. Our intension is to capture the primary reflections from the interfaces 1, 2, and 3. Therefore, the dimension of each layer along the x axis is calculated based on the

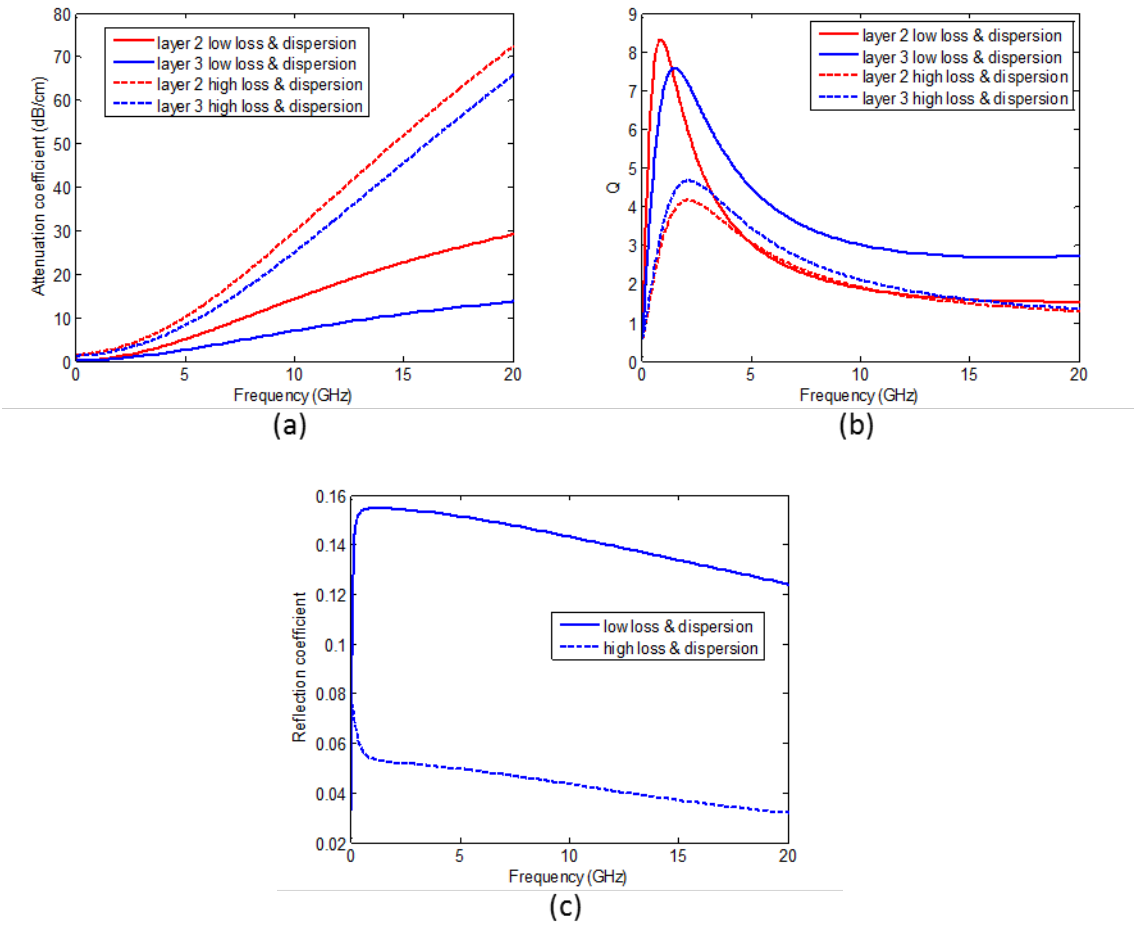

Fig. 6. The frequency dependent behavior of the lossy dispersive layers: (a) the attenuation coefficients, (b) the Q, and (c) the reflection coefficients at Interface 2.

given dielectric properties in order to exclude the multiples in the simulated data.

Two variations of source wavelets are tested. The first one is the minimum phase equivalent of the differentiated Gaussian pulse defined as

$$w(t) = (t - t_0)e^{-\frac{(t-t_0)^2}{\tau^2}}, \tag{34}$$

in which $t_0 = 0.25\,ns$ and $\tau = 0.0625\,ns$. The minimum phase wavelet is estimated by the use of cepstral method. The second one is a Ricker wavelet obtained by taking the differential of $w(t)$.

Breast phantom reflection measurements

Reflection measurements are acquired with a breast phantom in order to assess the performance of Gabor nonstationary deconvolution in a more realistic application. The data are collected using the TSAR breast imaging system (Fear et al., 2013), which incorporates an ultra-wideband (UWB) sensor, namely the BAVA-D antenna (Bourqui, 2008). The BAVA-D sensor is developed for near-field microwave imaging and sensing.

It is designed to operate in a specific background medium, i.e., canola oil, in which the BAVA-D sensor

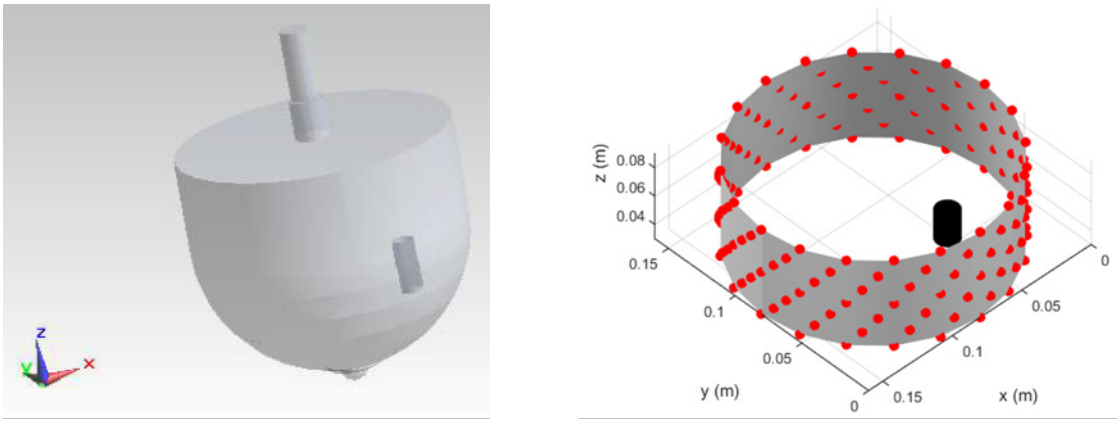

Fig. 7. The structure of the breast phantom (a) and the acquisition geometry (b). The red dots represent the antenna, and the black cylinder represents the tumor.

is able to produce a narrow beamwidth and generally high fidelity while keeping the return loss below -10 dB between 2.4 to 18 GHz.

Figure 7(a) shows the structure of the breast phantom. It is a dispersive homogeneous medium with effective permittivity $\varepsilon_{eff}(\omega) = 15$ and effective conductivity $\sigma_{eff}(\omega) = 0.01\ S/m$, and contains a lossless cylindrical inclusion with $\varepsilon_{eff}(\omega) = 2.08$. In order to effectively couple the microwave signal into the imaged object, the antenna and the phantom were placed in a tank filled with the canola oil. The dielectric properties of canola oil are $\varepsilon_{eff}(\omega) = 2.5$ and $\sigma_{eff}(\omega) = 0.04\ S/m$. The antenna position relative to the tumor inclusion is illustrated in Figure 7(b). During the phantom scan, the antenna behaved as both transmitter and receiver, i.e., monostatic radar. The antenna is repositioned over a cylindrical surface (in gray). Along the z direction, the antenna scanned through seven vertical positions from the nipple to the chest wall. At each vertical location, the antenna rotated around the breast phantom and collected data from 20 different locations. In total, 140 measurements were collected. The current TSAR processing flow (Fear et al., 2013) is utilized for data analysis and image reconstruction. The steps are described in Table 2.

RESULTS AND DISCUSSIONS

Of importance in this paper is to examine the ability of Gabor nonstationary deconvolution to handle the frequency-dependent attenuation and dispersion in EM wave propagation over microwave frequencies. The results presented in this section are to demonstrate the algorithm effectiveness in this regard.

Uniform plane wave propagation in lossy dispersive media

Following the steps described in Table 1, we generate the synthetic data to simulate the uniform plane wave propagation in various lossy dispersive body tissues. In the example shown in Figure 8, the tissue has the same dielectric properties as the one illustrated in

Figure 1. The model structure is described by the top signal in Figure 8. With this model, our intention is to test the ability of the Gabor algorithm to 1) separate the superposed wavelets and 2) recover the weak response later in time that contain a great amount of

Table 2. Steps of data processing and image reconstruction

1) *Remove the antenna response from recorded data*. Two sets of data are recorded, one with and one without the presence of an object. The object reflections are calibrated by subtracting the antenna only response from the data recorded with the presence of object.
2) *Convert frequency recordings to time signals.* Given a pulse specified in time domain, a chirp z-transform (Ulriksson, 1986) is used to find its frequency representation at the measured frequencies. The frequency measurements are weighted with the frequency spectrum of the given pulse. Finally, the inverse chirp z-Transform is used to convert the weighted frequency recordings from frequency domain to time domain.
3) *Correct time zero to the antenna aperture location*. Estimate the antenna aperture location in the signal by following the approach described in (Liu et al., 2015). Clip off the signal prior to the estimated antenna aperture.
4) *Deconvolve the signals.* Apply Gabor nonstationary deconvolution to the signals.
5) *Reconstruct images*. Image reconstruction is performed using the confocal imaging approach (i.e., Kirchhoff migration) described in (Fear et al., 2013).

attenuation and dispersion. The synthesized attenuated signal is shown at the bottom of Figure 8. We process the synthetic signal with Gabor nonstationary deconvolution and Wiener stationary deconvolution. There are two variations with the Gabor deconvolution depending on the construction of the hyperbolic contours for attenuation function estimation. In one case, the hyperbolic contours are constructed using the constant Q model; in the other case, they are constructed using the frequency-dependent Q model.

The results indicate that Gabor deconvolution gives a more accurate estimation of the true reflectivity than the stationary deconvolution. First of all, the Gabor estimates are able to separate the superposed wavelets and place the associated reflectivity in the proper locations. Secondly, the Gabor algorithm is able to detect the small reflectivity at late time and compensate for its energy dissipation. Moreover, the relative strengths of individual reflectivities are recovered with reasonably good accuracy. On the other hand, similar results are observed between the estimates obtained from the constant Q model and the frequency-dependent Q model. This indicates that the difference in the shape of hyperbolas constructed with different Q models does not significantly affect the overall accuracy of the Gabor estimate. With practical applications, it is impossible to construct the hyperbolas using frequency-dependent Q model since each medium has its own characteristics of frequency-dependency. Given the tested tissue (i.e., fat), the Q* is shown in Figure 3(d), which exhibits a good consistency over the frequencies of interest. This result provides us

with evidence that Gabor nonstationary deconvolution is feasible for the condition where a constant Q^* model can be approximated.

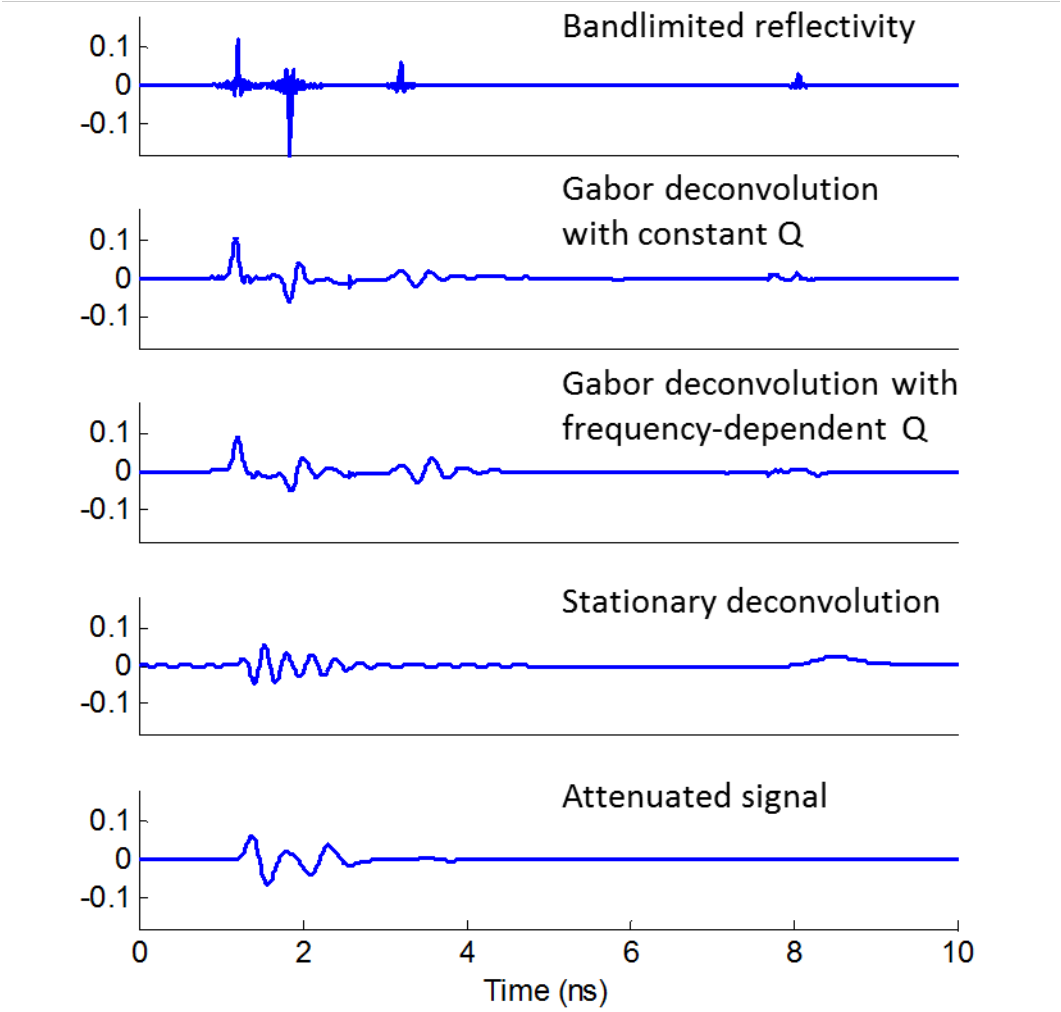

Fig. 8. The performance of Gabor nonstationary deconvolution with the synthetic signal to simulate the uniform plane wave propagation in a lossy dispersive body tissue. From top to bottom, the signals represent the true reflectivity, the output of the Gabor algorithm with the constant Q model, the output of the Gabor algorithm with the frequency-dependent Q model, the output of the Wiener deconvolution, and the attenuated signal, respectively.

Plane wave propagation in layered media

With the parallel plate wave guide simulations, Figure 9 shows the results obtained from the media that exhibit low and high levels of attenuation and dispersion. In each case, the middle two layers are assigned with the dielectric properties illustrated in Figure 6. The attenuated signals are shown in Figure 9(a), and the Gabor recovery of the reflectivity series are shown in Figure 9(b). In each figure, the signals with recording time less than 8 ns are obtained from the media with low loss and low dispersion, and the signals with recording time more than 8 ns are obtained from the media with high loss and high dispersion. The blue '*' indicates the expected locations of interfaces on signals. The obtained results reveal great promise of applying Gabor nonstationary deconvolution in the condition that

includes a large amount of attenuation and dispersion. In all cases, three reflections are supposed to be observed in the signal. However, before Gabor deconvolution, only the first reflection is visible in the attenuated signal, while the second and the third reflections have

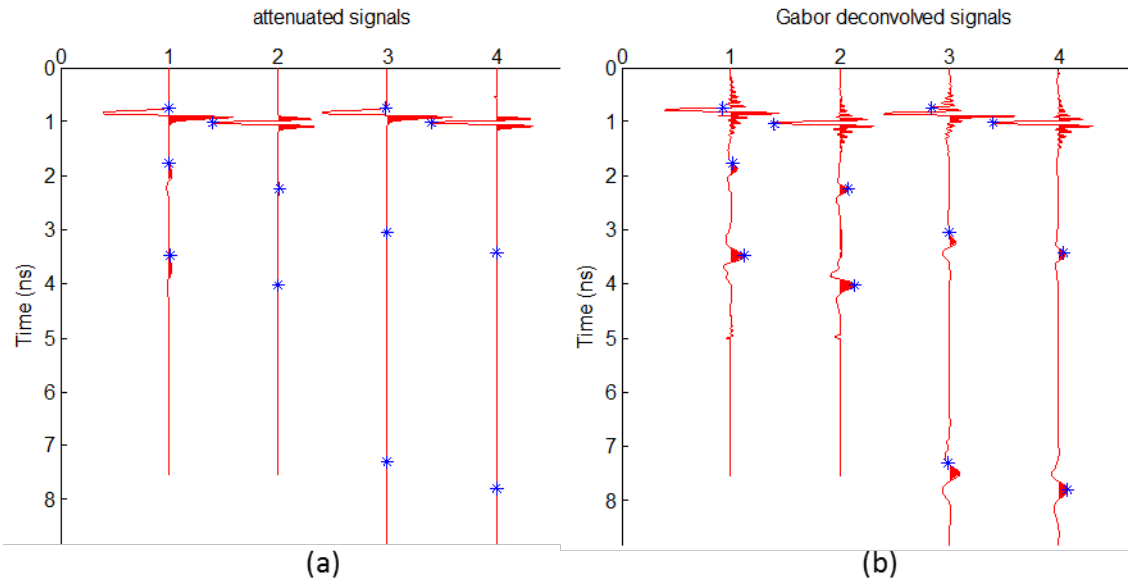

Fig. 9. Applying the Gabor deconvolution to the plane wave simulations. In each figure, the signals 1 and 2 are generated with low loss and low dispersion media using minimum phase source pulse and Ricker source pulse, respectively; the signals 3 and 4 are generated with high loss and high dispersion media using minimum phase source pulse and Ricker source pulse, respectively.

been greatly reduced to a level that is not noticeable. On the other hand, after Gabor deconvolution, the energy attenuation in the signal is sufficiently compensated, so that the responses at the second and the third interfaces can be clearly observed. These results indicate that the Gabor algorithm is able to detect the reflectivity from largely attenuated and distorted signals and place the reflectivity at the right location.

However, the under / over compensation is also observed in the Gabor estimates. We calculate the reflectivity at the each interface based on the given dielectric properties and the model geometrical structure and compare them with the Gabor estimates. There are differences observed between the Gabor estimates and the analytical calculations. Based on our observations, the under / over compensation often relates to (1) the size of the Gaussian partition window in terms of the time interval from the centre point to the $1/e$ amplitude point; and (2) the length of the boxcar filter in time and frequency dimensions for smoothing the Gabor amplitude spectrum. With a small-sized Gaussian window, the second reflection might be overly compensated and noise might be introduced at a later time, which in turn will overwhelm the actual response of the third interface. Given the tested datasets, the size of Gaussian partition window is chosen as at least one and half times the length of the source pulse. On the other hand, increasing the length of the boxcar filter in the time dimension might cause under compensation of the second reflection, without significantly affecting the recovery of the last reflection. Increasing the length of the boxcar filter in frequency dimension might cause over compensation of the third reflection in the signal, without significantly affecting the recovery of the second reflection.

Given the tested dataset, the optimal definitions for the time smoother and the frequency smoother are 1 ns and 1 GHz, respectively.

Despite these estimation errors, the Gabor recovered reflectivity series still provides much more information with respect to the object geometrical structure and physical properties than the unprocessed signal does. On the other hand, none of these lossy dispersive media has a constant Q over the simulation frequency band (1 – 15 GHz); however, they all have a relative constant Q*. In this regard, these results provide us with evidence that Gabor nonstationary deconvolution can work with the constant Q* model.

Gabor nonstationary deconvolution as preconditioning for image

With the breast phantom shown in Figure 7, the reflection measurements are collected to reconstruct the 3D breast image. Following the steps provided in Table 2, we apply Gabor nonstationary deconvolution and Wiener stationary deconvolution to the signals prior to image formation. We compared the reconstructed images with and without deconvolution as preconditioning. The results are shown in Figure 10.

All three images can detect the existence of the object of interest (i.e., tumor) at the accurate location. The image with Gabor deconvolution as preconditioning shows the best localization effect (i.e., the sharpness of the imaged object), while the image reconstructed with the data without deconvolution shows the least localization effect, and the image with the stationary deconvolution is in between. A slightly higher background noise may be observed in the image with Gabor deconvolution. This is because the Gabor algorithm is not able to differentiate the noise from the data. When compensating for the wave attenuation, the Gabor algorithm may also boost up the noise mixed together with the data. This noise might be reduced by applying a low pass filter to the post Gabor signal; however, there is always a tradeoff between improving the image resolution and decreasing the noise level.

Overall, modest improvement in the image resolution is observed in the result obtained with using Gabor nonstationary deconvolution as preconditioning for an image. Given this set of test data, several factors can limit the impact of Gabor nonstationary deconvolution on the final results. First, with this breast phantom, the tumor is embedded in the medium that has low loss and low dispersion. As the wave propagates in this medium, the distortion in the propagating wavelet is not significant. In other words, the propagating wavelet is similar to the source wavelet. Therefore, a stationary wave propagation can be approximated. This explains why stationary deconvolution also works in this case. Secondly, using the current flow of data processing and image reconstruction, after removing the skin response, only the tumor response is left in the signal. The basic idea of Gabor deconvolution is to use the strong response recorded at the early travel time as a reference to boost up the weak response recorded at the late travel time based on the Q characterization of wave attenuation. If there is only one response in the signal, no reference response is available to compensate for the attenuation. Moreover, the signal with only one response can be sufficiently handled by stationary deconvolution. In this regard, we have tested a simulation model by applying Gabor nonstationary deconvolution before

removing the strong skin response so that it can be used as a reference to compensate for the tumor response. The results will be presented in the future publications.

CONCLUSION

In this report, we extended the application of Gabor nonstationary deconvolution from seismic imaging to microwave imaging. The latter involves the microwave frequency EM

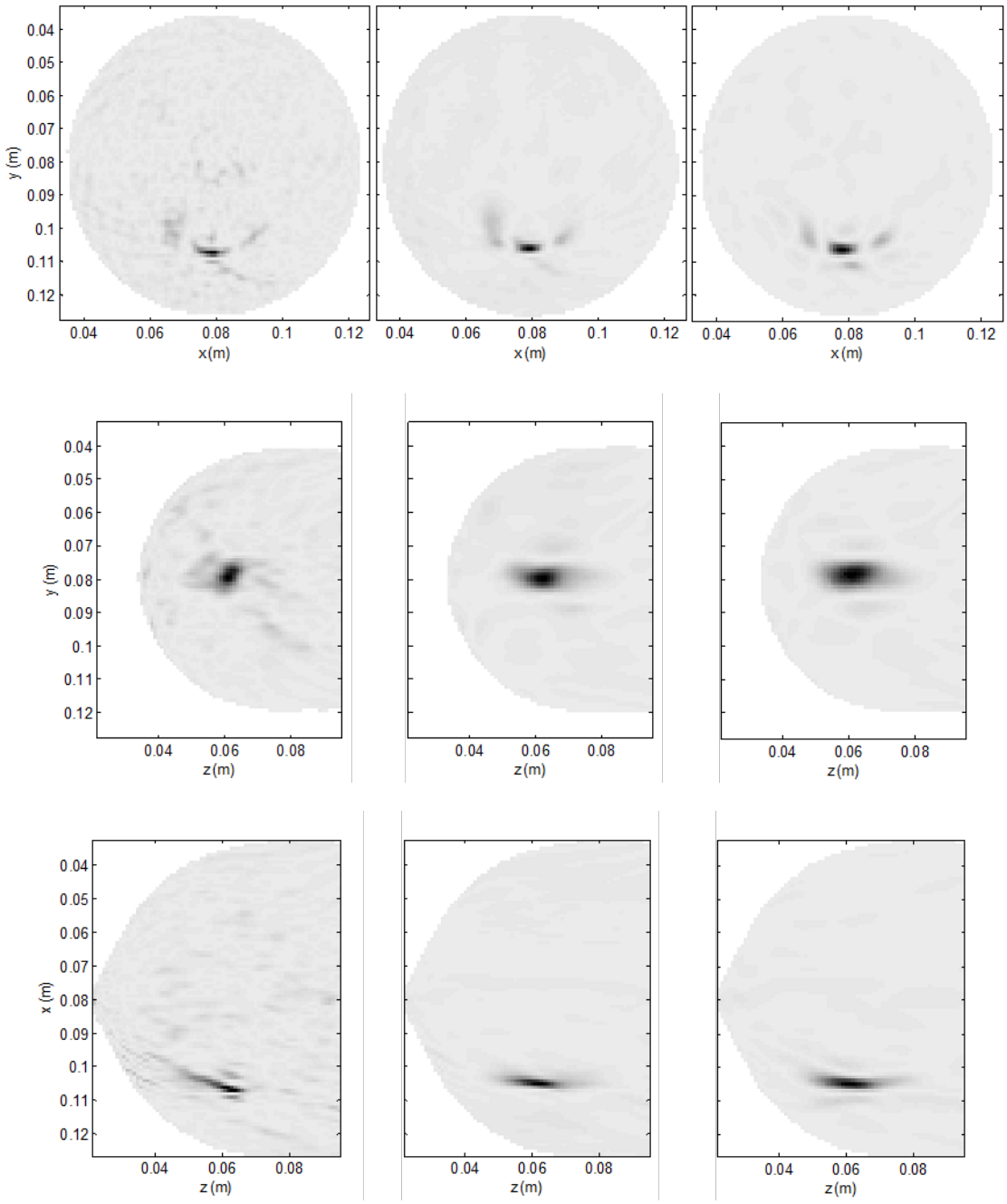

Fig. 10. Time focusing at the location of the maximum response in the image. From left to right, the images are reconstructed using Gabor nonstationary deconvolution as preconditioning, using

stationary deconvolution as preconditioning, and without deconvolution. From top to bottom, the images are sliced through the xy plane, the yz plane, and the xz plane, respectively.

wave propagation in biological media that have high attenuation and dispersion. We provided evidence that the same definition of Q as in the seismic can also be derived for EM waves. We calculated the Q for a variety of biological tissues over the microwave frequencies. The results indicate that the Q is in the range of [1.5, 8], more than one order of magnitude smaller than the Q observed in seismic. However, the results also indicate that the Q varies with frequency and a constant Q approximation might not be valid in this case. Fortunately, a new parameter Q* can be derived from Q, which shows more consistency over the microwave frequencies than the Q does. Even though Q and Q* might be different in the total magnitude, they describe the wave attenuation and dispersion in the same manner.

We tested Gabor deconvolution with analytical data, simulated data, and phantom measurements collected with EM propagation in highly attenuating and dispersive media. The results imply that Gabor deconvolution is able to deal with a Q that is much smaller than the seismic Q. With the analytic data, we compared the Gabor recovery of the object reflectivity obtained from the constant Q model and the frequency-dependent Q model. The results indicate that the difference in the hyperbolic contours constructed with different Q models does not significantly affect the Gabor estimate. With the simulation of plane wave propagation through layered media, the Gabor deconvolution is able to boost up the reflectivity from a weak response at its correct location even though the relative amplitude is slightly off from the analytical calculation given the dielectric properties. With the phantom measurements, the image with Gabor deconvolution as preconditioning shows better target localization than the images obtained from stationary deconvolution and unprocessed data. However, since the tested phantom includes a single target and is made from a material of low loss and low dispersion, the difference in the images with and without Gabor deconvolution as preconditioning is not significantly large. Moreover, since Gabor deconvolution is not designed to distinguish between noise and data, the algorithm may unintentionally boost up the noise when compensating for attenuation. Thus, noise attenuation should be performed prior to the Gabor deconvolution.

Several priorities of our future work are defining (1) the proper phantom models to be able to best test the Gabor algorithm and (2) the necessary steps to integrate the Gabor algorithm into the current workflow of microwave imaging.

ACKNOWLEGEMENT

This work is financially supported by the Natural Sciences and Engineering Research Council of Canada (NSERC), the Alberta Innovates Technology Futures (AITF), NSERC Collaborative Research and Training Experience (CREATE) Program, and the University of Calgary. The authors are grateful to David Henley for sharing his understanding and insights in Gabor nonstationary deconvolution, and deeply appreciate his comments and suggestions. The authors thank Jeremie Bourqui for his help on antenna measurement systems. Finally, the authors wish to thank the Consortium for Research in Elastic Wave Exploration Seismology (CREWES) for providing the software support.

REFERENCES

Aki, K., and Richards, P. G., 2002, Quantitative Seismology: Theory and methods. University Science Books.

Bano, M., 1996, Constant dielectric losses of ground-penetrating radar waves: Geophysical Journal International, 124, 279-288.

Bradford, J. H., 2007, Frequency-dependent attenuation analysis of ground-penetrating radar data: Geophysics, 72, J7-J16.

Bourqui, J., 2008, Balanced antipodal Vivaldi antenna and dielectric director for breast cancer detection, University of Calgary, Calgary, Alberta, Canada.

Fear, E. C., Bourqui, J., Curtis, C., Mew, D., Docktor, B., and Romano, C., 2013, Microwave Breast Imaging With a Monostatic Radar-Based System: A Study of Application to Patients: IEEE Transaction on Microwave Theory and Techniques, 61, 2119-2128.

Gabriel, S., Lau, R. W., and Gabriel, C., 1996, The dielectric properties of biological tissues .3. Parametric models for the dielectric spectrum of tissues: Physics in Medicine and Biology, 41, 2271-2293.

Von Hippel, A. R., 1954, Dielectrics and Waves. John Wiley & Sons, Inc.

Irving, J. D., and Knight, R. J., 2003, Removal of wavelet dispersion from ground-penetrating radar data: Geophysics, 68, 960-970.

Kjartansson, E., 1979, Constant Q-wave propagation and attenuation: Journal of Geophysical Research, 84, 4737-4748.

Lazebnik, M., McCartney, L., Popovic, D., Watkins, C. B., Lindstrom, M. J., Harter, J., et al., 2007, A large-scale study of the ultrawideband microwave dielectric properties of normal breast tissue obtained from reduction surgeries: Physics in Medicine and Biology, 52, 2637-2656.

Liu, K. Y., Fear, E., and Potter, M., 2015, Antenna aperture localization for arrival time correction using first-break: Progress In Electromagnetics Research B, *62*, 105-120.

Margrave, G. F., Lamoureux, M. P., and Henley, D. C., 2011, Gabor deconvolution: Estimating reflectivity by nonstationary deconvolution of seismic data: Geophysics, 76, W15-W30.

Margrave, G. F., Henley, D. C., Lamoureux, M. P., Iliescu, V., and Grossman, J. P., 2002, A update on Gabor deconvolution: CREWES Research Report, 14.

Margrave, G. F., Dong, L., Gibson, P., Grossman, J., Henley, D., and Lamoureux, M., 2003, Gabor deconvolution: Extending Wiener's method to non-stationarity: CREWES Research Report, 15.

Perz, M., Mewhort, L., Margrave, G. F., and Ross, L., 2005, Gabor deconvolution: Real and synthetic data experiences: CSEG Convention Expanded Abstracts.

Pozar, D. M., 2005, Microwave Engineering. John Wiley & Sons, Inc.

Sheriff, R. E., 1984, Encyclopedic Dictionary of Exploration Geophysics. Society of Exploration Geophysics.

Stacey, F. D., Gladwin, M. T., McKavanagh, B., Linde, A. T., and Hastie, L. M., 1975, Anelastic damping of acoustic and seismic pulses: Geophysical Surveys, 2, 133-151.

Taflove, A., and Hagness, S. C., 2000, Computational Electrodynamics: The Finite-Difference Time-Domain Method. Artech House.

Turner, G., and Siggins, A. F., 1994, Constant Q-attenuation of subsurface radar pulses: Geophysics, 59, 1192-1200.

Ulriksson, B., 1986, Conversion of frequency-domain data to the time domain: Proceedings of the IEEE, 74, 74-77.

Wang, Y., 2008, Seismic Inverse Q Filtering. Blackwell Publishing.